Simulations of fast component and slow component of SMBI on HL-2A tokamak*

Yong-Fu Shi(史永福)[1], Zhan-Hui Wang(王占辉)[1,†], Qi-Long Ren(任启龙)[2,‡], Ai-Ping Sun(孙爱萍)[1], De-Liang Yu(余德良)[1], Wen-Feng Guo(郭文峰)[2], and Min Xu(许敏)[1]

[1] *Southwestern Institute of Physics, Chengdu* 610041, *China*
[2] *Institute of Plasma Physics, Chinese Academy of sciences, Hefei* 230031, *China*

(Received 15 November 2016; revised manuscript received 22 January 2017; published online 30 March 2017)

It is very important to improve the penetration depth and fueling efficiency of supersonic molecular beam injection (SMBI) especially for the next generation fusion devices such as ITER. Two components, a fast component (FC) and a slow component (SC), have been observed in the HL-2A SMBI experiments for several years, and the FC can penetrate much more deeply than the common SMBIs which draws a great deal of attention for a better fueling method. It is the first time to the FC and SC of SMBI have been simulated and interpreted in theory and simulation in this paper with the trans-neut module of the BOUT++ code. The simulation results of the FC and SC are clear and distinguishable in the same way as the observation in experiment. For the major mechanism of the FC and SC, it is found that although the difference in the injection velocity has some effect on the penetration depth difference between the FC and SC, it is mainly caused by the self-blocking effect of the first ionized SMB. We also discuss the influence of the initial plasma density on the FC and SC, and the variation of the SC penetration depth with its injection velocity.

Keywords: supersonic molecular beam injection, fast component and slow component, penetration depth, self-blocking effect

PACS: 52.25.Fi, 52.25.Ya **DOI:** 10.1088/1674-1056/26/5/055201

1. Introduction

It is important to improve the penetration depth and efficiency of plasma fuelling for controlling the plasma density and studying plasma physics especially in the next generation fusion devices such as ITER. There are three major fueling methods: gas puffing (GP),[1] pellet injection (PI),[2] and supersonic molecular beam injection (SMBI).[3] GP is the simplest and most traditional method with the lowest fuelling efficiency and the shallowest penetration depth. PI can penetrate into the core plasma but costs a lot for its complex structure and technology. SMBI costs less than PI because of its simpler structure and technology, and its fuelling efficiency is about three to four times as high as that of GP.[4] The key technique difference between SMBI and GP is the Laval nozzle of SMBI. It leads to a directed group fluid velocity of molecules during SMBI, which is very different from the individual isotropic thermal speed of molecules during GP. An improved SMBI with clusters, which are like micro-pellets, can be injected more deeply.[5] Besides being used in the plasma fuelling, SMBI can also be applied to study plasma impurity transport,[6–8] L–H transition and confinement improvement,[9–11] edge localized mode (ELM) mitigation,[12–18] and nonlocal heat transport.[19–22]

Since the fuelling efficiency depends on the penetration depth, some experiments have been carried out to improve the SMBI penetration depth on the HL-2A tokamak.[4,23,24] The SMBI fuelling depth can be measured with electron-cyclotron emission, soft x-ray diagnostics, D_α array, and CCD camera on the HL-1M and HL-2A,[24–27] fast TV camera and charge exchange recombination spectroscopic in JT-60U.[28,29] The penetration characteristics of SMBI studied by D_α array and CCD camera on HL-2A showed that the SMBI from the low field side consists of a slow component (SC) and a fast component (FC). The FC can penetrate more deeply than the common SMBI, and it is about 4–5 cm deeper than the SC.[23] It is the observation of FC that greatly draws our attention to develop a new method of SMBI for deeper penetration and higher efficiency. Although the FC and SC have been studied experimentally for many years, there is little research in theory and simulation to interpret it. In order to study the penetration mechanism and characteristic of the FC and SC, a module (named trans-neut) of the BOUT++ [30] code is used to simulate their penetration processes. Trans-neut is a module developed for studying the time-dependent three-dimensional (3D) neutrals and plasmas transport dynamics during fueling of SMBI or GP in real tokamak geometries.[31] It can be used to simulate, understand, and predict SMBI experiments, and

*Project supported by the National Natural Science Foundation of China (Grant Nos. 11575055, 11375053, and 11472519), the Chinese National Fusion Project for ITER (Grant Nos. 2013GB111005, 2013GB107001, 2014GB108004, 2014GB110004, and 2015GB110001), and the International S&T Cooperation Program of China (Grant No. 2015DFA61760).

†Corresponding author. E-mail: zhwang@swip.ac.cn
‡Corresponding author. E-mail: renql@ipp.ac.cn

© 2017 Chinese Physical Society and IOP Publishing Ltd

its simulation results are in good agreement with the experimental data.[32] With the module, the injection efficiency and depth have been compared between tokamak fuellings of GP and SMBI,[33] and the molecular penetration depth variation with the SMBI fluxes has also been studied.[34] A new one-dimensional (1D) code named TPSMBI has also been developed recently based on a six-field SMBI model in the cylindrical coordinate and it has been benchmarked well with the trans-neut module of the BOUT++ code.[35]

In this paper, the D_α intensity is calculated by using the data in the atomic data and analysis structure (ADAS) database of the photon emissivity coefficient of D_α, which is related to the plasma density and electron temperature.[36] The simulation results will be compared with the experiments by calculating the D_α intensity. We will further study the major mechanism of the FC and SC, the influence of the initial plasma density on the FC and SC, and the influence of the injection velocity on the SC for the underlying physics. The remainder of this paper is organized as follows. The physical model is briefly described in Section 2. Numerical initial conditions and boundary conditions are shown in Section 3. The simulation results are illustrated in Section 4. Finally, the main results are summarized in Section 5.

2. Physical model

A seven-field fluid model, which couples plasma density N_i, temperatures T_e and T_i, and parallel velocity $V_{\|\mathrm{i}}$ transport equations together with neutrals densities of both molecules N_m and atoms N_a and molecule radial velocity $V_{x\mathrm{m}}$ transport equations, has been developed in Ref. [31] by the reduction of the Braginskii equations[37] with source and sink terms. The physical equations of the model are introduced as follows:

$$\frac{\partial N_\mathrm{i}}{\partial t}+\nabla_\|\left(V_{\|\mathrm{i}}N_\mathrm{i}\right)-D^\mathrm{c}_{\perp\mathrm{i}}\nabla^2_\perp N_\mathrm{i}=S^\mathrm{p}_\mathrm{I}-S^\mathrm{p}_\mathrm{rec}, \tag{1}$$

$$\begin{aligned}&\frac{\partial T_\mathrm{e}}{\partial t}-\frac{2}{3N_\mathrm{i}}\nabla_\|\left(\kappa^\mathrm{c}_{\|\mathrm{e}}\nabla_\|T_\mathrm{e}\right)-\frac{2}{3}\chi^\mathrm{c}_{\perp\mathrm{e}}\nabla^2_\perp T_\mathrm{e}\\&=\nu_\mathrm{rec}W_\mathrm{rec}-\nu_\mathrm{I}\left(T_\mathrm{e}+\frac{2}{3}W_\mathrm{I}\right)-\frac{2}{3}\nu_\mathrm{diss}\left(W_\mathrm{diss}+W_\mathrm{bind}\right)\\&\quad-\frac{2m_\mathrm{e}}{M_\mathrm{i}}\frac{T_\mathrm{e}-T_\mathrm{i}}{\tau_\mathrm{e}},\end{aligned} \tag{2}$$

$$\begin{aligned}&\frac{\partial T_\mathrm{i}}{\partial t}+V_{\|\mathrm{i}}\nabla_\|T_\mathrm{i}+\frac{2}{3}T_\mathrm{i}\nabla_\|V_{\|\mathrm{i}}\\&\quad-\frac{2}{3N_\mathrm{i}}\nabla_\|\left(\kappa^\mathrm{c}_{\|\mathrm{i}}\nabla_\|T_\mathrm{i}\right)-\frac{2}{3}\chi^\mathrm{c}_{\perp\mathrm{i}}\nabla^2_\perp T_\mathrm{i}\\&=\left(\nu_\mathrm{rec}-\nu_\mathrm{I}\right)T_\mathrm{i}+\frac{2m_\mathrm{e}}{M_\mathrm{i}}\frac{T_\mathrm{e}-T_\mathrm{i}}{\tau_\mathrm{e}},\end{aligned} \tag{3}$$

$$\begin{aligned}&\frac{\partial V_{\|\mathrm{i}}}{\partial t}+V_{\|\mathrm{i}}\nabla_\|V_{\|\mathrm{i}}-\frac{4}{3N_\mathrm{i}M_\mathrm{i}}\nabla_\|\left(\eta_{\mathrm{i}\|}\nabla_\|V_{\|\mathrm{i}}\right)\\&=-\frac{\nabla_\|P}{N_\mathrm{i}M_\mathrm{i}}-\left(\nu_\mathrm{CX}-\nu_\mathrm{I}\right)V_{\|\mathrm{i}},\end{aligned} \tag{4}$$

$$\begin{aligned}&\frac{\partial N_\mathrm{a}}{\partial t}-\nabla_\|\left(D^\mathrm{c}_{\|\mathrm{a}}\nabla_\|N_\mathrm{a}\right)-D^\mathrm{c}_{\perp\mathrm{a}}\nabla^2_\perp N_\mathrm{a}\\&=-S^\mathrm{p}_\mathrm{I}+S^\mathrm{p}_\mathrm{rec}+2S^\mathrm{p}_\mathrm{diss},\end{aligned} \tag{5}$$

$$\frac{\partial N_\mathrm{m}}{\partial t}+\nabla_x\left(V_{x\mathrm{m}}N_\mathrm{m}\right)=-S^\mathrm{p}_\mathrm{diss}, \tag{6}$$

$$\frac{\partial V_{x\mathrm{m}}}{\partial t}+V_{x\mathrm{m}}\nabla_xV_{x\mathrm{m}}=-\frac{\nabla_xP_\mathrm{m}}{N_\mathrm{m}M_\mathrm{m}}. \tag{7}$$

Equations (1)–(4) describe the transport of plasma density N_i, ion and electron temperatures T_e and T_i, and ion parallel velocity $V_{\|\mathrm{i}}$, respectively. $D^\mathrm{c}_{\perp\mathrm{i}}$, $\chi^\mathrm{c}_{\perp\mathrm{e}}$, and $\chi^\mathrm{c}_{\perp\mathrm{i}}$ are perpendicular classical diffusion coefficients of plasma density, electron temperature, and ion temperature, respectively. $\kappa^\mathrm{c}_{\|\mathrm{e}}$ and $\kappa^\mathrm{c}_{\|\mathrm{i}}$ are parallel classical thermal conductivity coefficients of electron and ion. S^p_I is the atom ionization source, and $S^\mathrm{p}_\mathrm{rec}$ is the ion and electron recombination sink of plasma density. ν_rec, ν_I, ν_diss, and ν_CX are the plasma recombination rate, atom ionization rate, molecule dissociation rate, and ion–atom charge exchange rate, respectively. W_rec is the fraction of the recombination energy re-absorbed by electrons during recombination, W_I and W_diss are the electron energy lost per ionization and dissociation, and W_bind is the binding energy between the two hydrogen atoms in a molecule. τ_e is the electron–ion collision time and $\eta_{\mathrm{i}\|}$ is the parallel ion viscosity. P is the total plasma pressure. Equation (5) is the atom density transport equation, where $D^\mathrm{c}_{\|\mathrm{a}}$ and $D^\mathrm{c}_{\perp\mathrm{a}}$ are the parallel and perpendicular atom diffusion coefficients, and $S^\mathrm{p}_\mathrm{diss}$ is the atom source due to molecule dissociation. Equations (6) and (7) are molecule density N_m and radial velocity $V_{x\mathrm{m}}$ transport equations. P_m is the molecule pressure. The molecule temperature is chosen to be the room temperature (i.e., 300 K). The symbol ∇_x represents the radial component of the gradient. More details of the physical model can be found in Ref. [31].

3. Numerical initial and boundary conditions

3.1. Numerical initial conditions

In order to do the simulation and comparison with HL-2A experiments, a real HL-2A tokamak geometry of shot #9940 at 221 ms just before the first SMBI pulse is used in the simulation according to the first observation of FC and SC in Ref. [23]. Unfortunately, because the experimental data of plasma density and temperature profiles have been lost, the numerical initial profiles of plasma density and temperatures are selected to be characteristic linear profiles based on the measurement of line-averaged electron density and electron temperature in the core. The plasma density and electron temperature profiles are shown in Fig. 1. The plasma density is normalized with a reference density $N_0=1\times10^{19}$ m^{-3}. The field-aligned coordinates with the normalized magnetic flux are applied in the trans-neut module and BOUT++ code. The quasi-neutral assumption of plasma is used in the simulation. The initial ion temperature profile is simply assumed to be the same as the initial electron temperature profile.

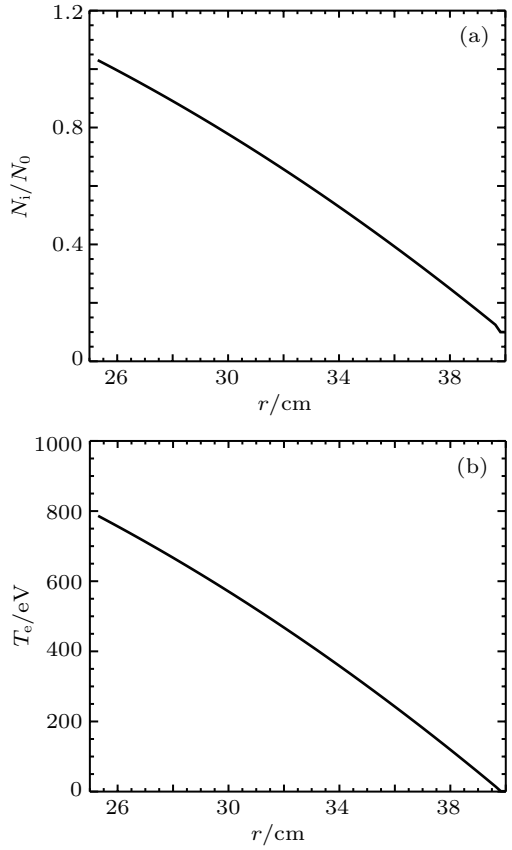


Fig. 1. Initial profiles used in the simulations: (a) the density and (b) the electron temperature.

3.2. Numerical boundary conditions

Numerical implementation of the boundary conditions is expressed in Ref. [31], including the radial flux-driven boundary condition, the particle recycling boundary condition, the SMBI localized boundary condition, and the sheath boundary condition. The field-aligned coordinates (x, y, z) are applied in the simulation, which are related to the usual flux coordinates $(\psi, \theta, \varsigma)$. The simulation range is normalized magnetic flux $\hat{\psi} = 0.4$–1.0 (minor radius r is about 25–40 cm). The physical quantities are normalized to the characteristic parameters, such as $L_0 = 2.14$ m (a reference length), $T_0 = 1$ keV (a reference plasma temperature), $V_0 = \sqrt{T_0/M_i}$ (ion thermal velocity at T_0), $t_0 = L_0/V_0$ (a thermal transport time), $N_0 = 1 \times 10^{19}$ m^{-3} (a reference plasma density at core), $M_0 = M_p$ (the mass of the proton), and $B_0 = 1.88$ T (the maximum of the magnetic field). At the innermost of the simulation range, the Neumann radial boundary conditions are set for all evolving quantities except for N_i, T_e, and T_i, which are given fixed-gradient or flux-driven boundary conditions as follows:

$$\left.\frac{\partial N_i}{\partial x}\right|_{\text{core}} = -C_{Ni}\frac{N_0}{L_0^2 B_0}, \tag{8}$$

$$\left.\frac{\partial T_{e,i}}{\partial x}\right|_{\text{core}} = -C_{Te,i}\frac{T_0}{L_0^2 B_0}, \tag{9}$$

where the coefficients $C_{Ni} = 230$ and $C_{Te,i} = 196.18$ are the input parameters and can be calculated from $C_{Ni} = \Gamma_i|_{\text{core}} L_0^2 B_0 / D_{\perp i}^c \sqrt{g^{11}} N_0$ and $C_{Te,i} = Q_{e,i}|_{\text{core}} L_0^2 B_0 / \frac{2}{3}\chi_{\perp e,i}^c N_i|_{\text{core}} \sqrt{g^{11}} T_0$. Here $\Gamma_i|_{\text{core}}$ and $Q_{e,i}|_{\text{core}}$ are the inflowing particle and heat fluxes at the innermost boundary flux surface on the core side, respectively. The inflowing particle flux $\Gamma_i|_{\text{core}} = -D_{\perp i}^c \partial N_i/\partial R\big|_{\text{core}}$ is poloidally dependent and is about $4N_0$m/s. The inflowing heat flux

$$Q_{e,i}|_{\text{core}} = -\frac{2}{3}\chi_{\perp e,i}^c N_i|_{\text{core}} \left.\frac{\partial T_{e,i}}{\partial R}\right|_{\text{core}}$$

is also poloidally dependent and is about 4kW/m^2. The radial derivatives in the flux coordinates can be converted into real-space coordinates by multiplying of $\sqrt{g^{11}}$=RB_θ as $\partial f/\partial R\big|_{\text{core}} = \sqrt{g^{11}}\partial f/\partial x\big|_{\text{core}}$. These flux-driven boundary conditions at the core represent continuously inflowing particle and heat fluxes, or ad hoc effective local sources of particle and heat that are necessary to maintain the plasma profiles at a steady state. At the outermost of the simulation, N_i, T_i, and T_e are fixed to their initial values. For all the evolving quantities, the pseudo-periodic boundary conditions are applied in the direction parallel to the magnetic field within the separatrix. The boundary conditions can be varied accordingly to the generated different initial plasma profiles and the influence on the FC and SC.

4. Simulation results

4.1. Calculation of D$_\alpha$ intensity

The penetration depth of SMBI is measured by D$_\alpha$ array in experiment and it is defined as the distance from the plasma edge to the maximum D$_\alpha$ intensity region. In the simulation, the spatio-temporal evolution of the D$_\alpha$ intensity is calculated as follows:[1]

$$I_{D_\alpha}(r,t) = q\left(N_i(r,t), T_e(r,t)\right) \times N_i(r,t) \times N_a(r,t), \tag{10}$$

where q is the photon emissivity coefficient of D$_\alpha$ and N_a is the density of deuterium atoms. q depends on both N_i and T_e.

D$_\alpha$ is the photon emitted when a deuterium atom jumps from the excited state of $n = 3$ to the excited state of $n = 2$, $D^*(n=3) \rightarrow D^*(n=2) + h\nu$. Deuterium atoms can reach the excited state of $n = 3$ through three processes: 1) electron-collision excitation, $e + D \rightarrow e + D^*$; 2) recombination radiation, $e + D^+ \rightarrow D^* + h\nu'$(continuous spectrum); 3) charge exchange, $D + D^+ \rightarrow D^+ + D^*$. The electron-collision excitation plays the dominant role within the parameter scope of this simulation in edge tokamak plasma. The calculation of the D$_\alpha$ intensity needs the ADAS database. ADAS is the most famous and widely used database to model the radiating properties of ions and atoms in plasmas. It can provide various data for particle collision reactions and plasma spectrum analysis in experiments and simulation codes (such as B2-IRENE, CHEAP, DIVIMP, EDGE2D, SANCO, and STRAHL).

To calculate the photon emissivity coefficient q, we first add together the coefficients of electron-collision excitation and recombination radiation to get a total value, then the cubic spline interpolation is carried out in the space of plasma density N_i and electron temperature T_e. According to Eq. (10), the D_α intensity is not only proportional to the density of deuterium atoms, but also depends on some other parameters. It means that the D_α intensity measurement is not a direct measurement of the deuterium atom. Therefore it needs to verify whether the distance from the plasma edge to the maximum D_α density region correctly reflects the real penetration depth of SMBI. Figures 2(a) and 2(c) show the spatio–temporal evolutions of the D_α intensity during SMBI with different plasma densities and injection velocities, respectively. Comparing Fig. 2(a) with Fig. 2(b), we can find that the penetration depth given by the D_α intensity is consistent with that of the atom density front propagation. It is the same in comparison of Fig. 2(c) with Fig. 2(d). In a word, it is credible that the distance from the plasma edge to the maximum D_α density region represents the SMBI penetration depth well.

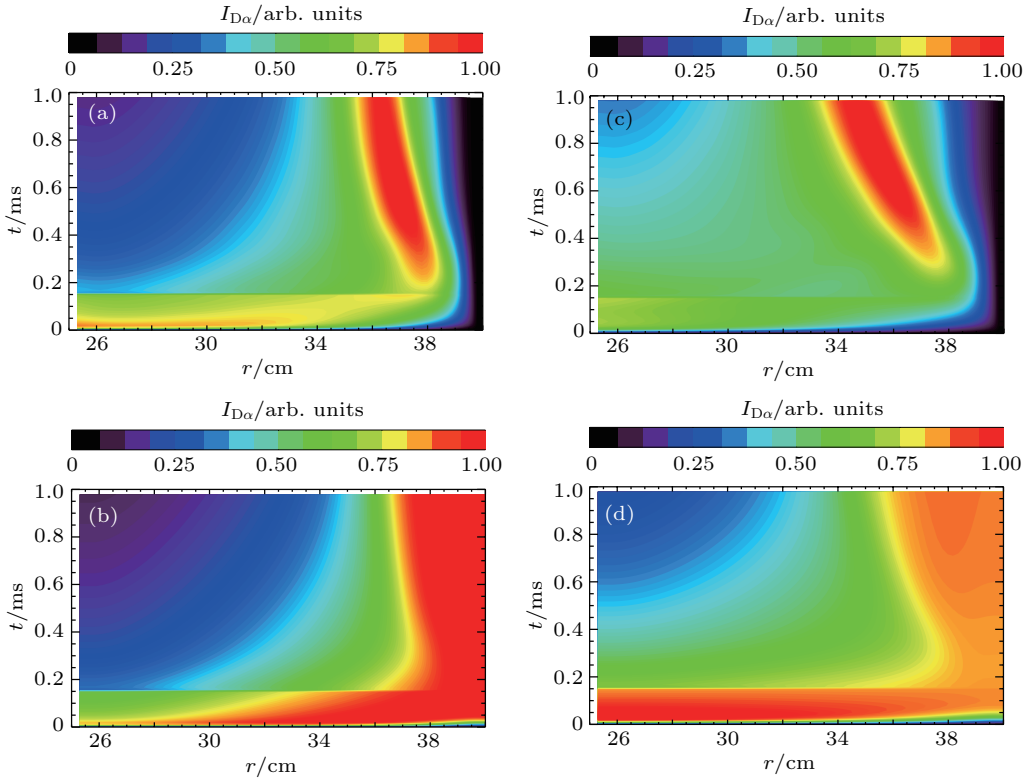


Fig. 2. (color online) The spatio–temporal evolutions of D_α intensity and atom density during SMBI for two different cases: (a) and (b) $N_i = 1.4N_0$; (c) and (d)$N_i = 0.6N_0$.

4.2. Simulation results of FC and SC

Both FC and SC are widely observed in lots of shots on the HL-2A tokamak. Figure 3 shows the first experimental observation of FC and SC (shots #9940 and #9897) on HL-2A. [23] Figures 3(a) and 3(b) exhibit the evolutions of electron density and D_α signals during eleven SMBI pulses. Figures 3(c) and 3(d) exhibit their evolutions during the first 1 ms SMBI pulse. It can be seen from Figs. 3(d) and 3(e) that there are two peaks in D_α signals evolution during SMBI injection, one small peak at 0.7 ms and one large peak at 1 ms. The earlier and faster molecular component of SMBI induces the first peak (i.e. the small peak) and is defined as the FC, while the latter following peak is larger and induced by the SC. The different penetration depths of the FC and SC are clearly shown in Fig. 3(f). Another FC and SC experiment on HL-2A (shot #9897) is shown in Fig. 4. It can be found from Fig. 4(b) that the FC can penetrate about 4–5 cm deeper than that the SC does.

In the experiments, the velocities of FC and SC are estimated by the distance from the nozzle to the plasma edge divided by the time intervals between the two peaks of the D_α signals and the SMBI triggering signal, respectively. According to the experimental results of shot #9940, we choose 1200 m/s and 800 m/s as the initial FC and SC injection velocities, respectively. A 1 ms SMBI pulse with a fast component and a slow component injects at the low field side of the HL-2A tokamak. Since the time interval between FC and SC is about 0.15 ms in the experiment, we make the SC injection 0.15 ms later than the FC in the simulation. The simulation results are shown in Fig. 5. Figure 5(a) exhibits the D_α intensity spatio–temporal distribution induced by the FC and SC injection. We can find in Fig. 5(a) that the FC and SC are clear and distinguishable.

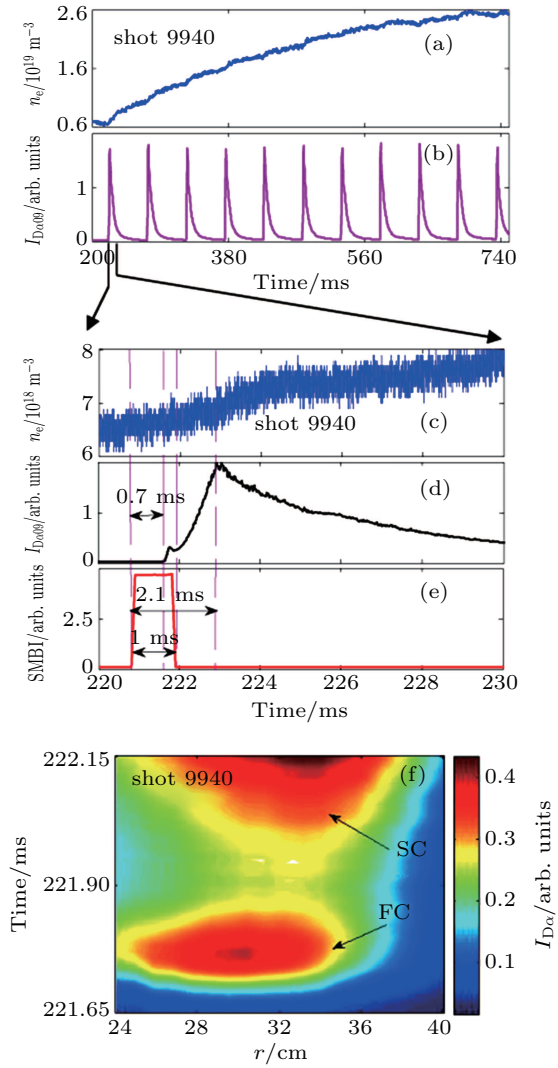


Fig. 3. (color online) The evolutions of electron density and corresponding D_α signals during SMBI pulses in shot #9940 on HL-2A. (a) and (b) The evolutions of line-averaged electron density and D_α signals during SMBI pulses, respectively. (c) and (d) the evolutions of line-averaged electron density and D_α signals during the first SMBI pulse, respectively. (e) the controlling signal of the first SMBI pulse. (f) contour plot for FC and a part of SC. Reprinted from Ref. [23] with permission.

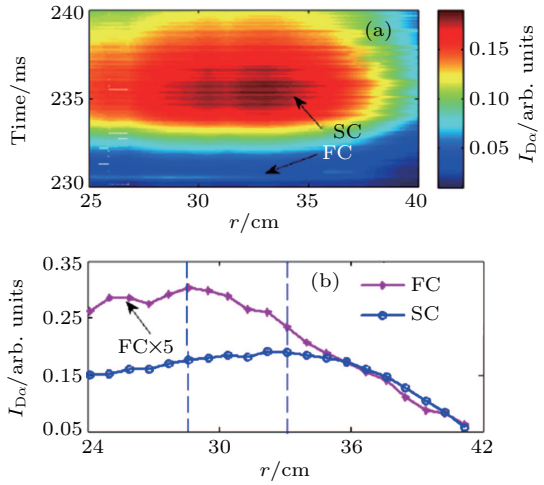


Fig. 4. (color online) Typical features of the FC and SC. (a) The spatio–temporal evolution of D_α intensity during the first SMBI in shot #9897 on HL-2A. (b) Radial profiles of D_α intensity for the FC and SC. Reprinted from Ref. [23] with permission.

Figure 5(b) shows the D_α intensity distributions in the radial direction. The black and red lines are the D_α intensity distribution produced by the FC and SC, respectively. It can be seen that the FC can penetrate about 4 cm deeper than the SC does. These are consistent with the experimental results.

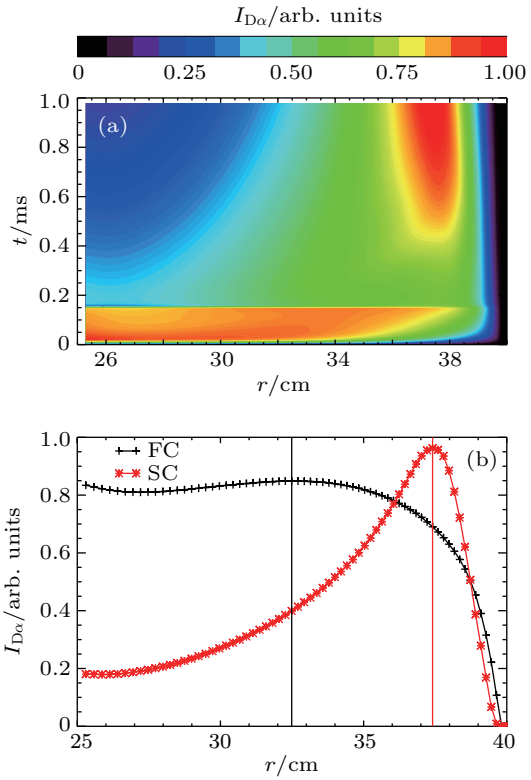


Fig. 5. (color online) Typical features of the FC and SC in simulation results. (a) The spatio–temporal evolution of D_α intensity during SMBI. (b) Radial profiles of D_α intensity produced by FC and SC.

4.3. Influence of the initial plasma density on FC and SC

In order to study the effect of the initial plasma density N_i on the injection of the FC and SC, we simulate their injection processes with different N_i. The simulation results are shown in Fig. 6. Figures 6(a)–6(d) show the D_α intensity induced by the FC and SC with N_i=0.6N_0, N_i= 1.0N_0, N_i=1.5N_0, and N_i= 2.0N_0 at the inner boundary ($r = 25$ cm), respectively. As shown in Fig. 6, the D_α intensities induced by the FC and SC are quite different. With the increase of the plasma density, the penetration depth of the FC becomes very shallow, while that of the SC is almost invariant. Similar results have been observed in the HL-2A experiments. In shot 9940, although the line-averaged electron density increases from 0.6×10^{19} m^{-3} to 2.6×10^{19} m^{-3} after 11 SMBI pulses, the penetration depth of the SC is almost unchanged.

4.4. Major mechanism of FC and SC

For a straightforward verification of the self-blocking effect on the penetration depth, the FC and SC are firstly supposed to be injected with the same velocity and then the FC is injected slower than the SC in the simulations.

In Ref. [23] , the analysis of experimental results shows that the difference in the penetration depth between FC and SC is mainly due to the self-blocking effect. In order to verify it, we use the same injection velocity 1200 m/s for the FC and SC in the simulation. The simulation results are shown in Fig. 7. Figure 7(a) shows the spatio-temporal evolution of the D_α intensity during SMBI. It can be seen that the penetration depth of SMBI is very deep in the first 0.1 ms but then it becomes shallow dramatically with the increase of the fueling time. In addition, we can find the difference of penetration deposition between FC and SC in Fig. 7(a). Figure 7(b) shows the radial profiles of D_α intensity for the FC and SC, respectively. It can be seen that the profiles of D_α intensity caused by the FC and SC are significantly different. Figure 7(c) shows the evolution of the radial plasma density profile at the injection path. It is clearly shown in Fig. 7(c) that there is a plasma density peak near the edge region and the peak grows large with SMBI injection. The peak has the self-blocking effect to block SMBI injecting deeply. For further verification, we reverse the injection velocities of the FC and SC to see whether a first but smaller injection velocity can make a deeper than the latter but faster one. The injection velocities of the FC and SC are 800 m/s and 1200 m/s, respectively. The simulation results are shown in Fig. 8. The FC can penetrate deeper than the SC even the velocity of the FC is slower than that of the SC. Therefore, the major mechanism of FC and SC is the self-blocking effect, rather than the injection velocity.

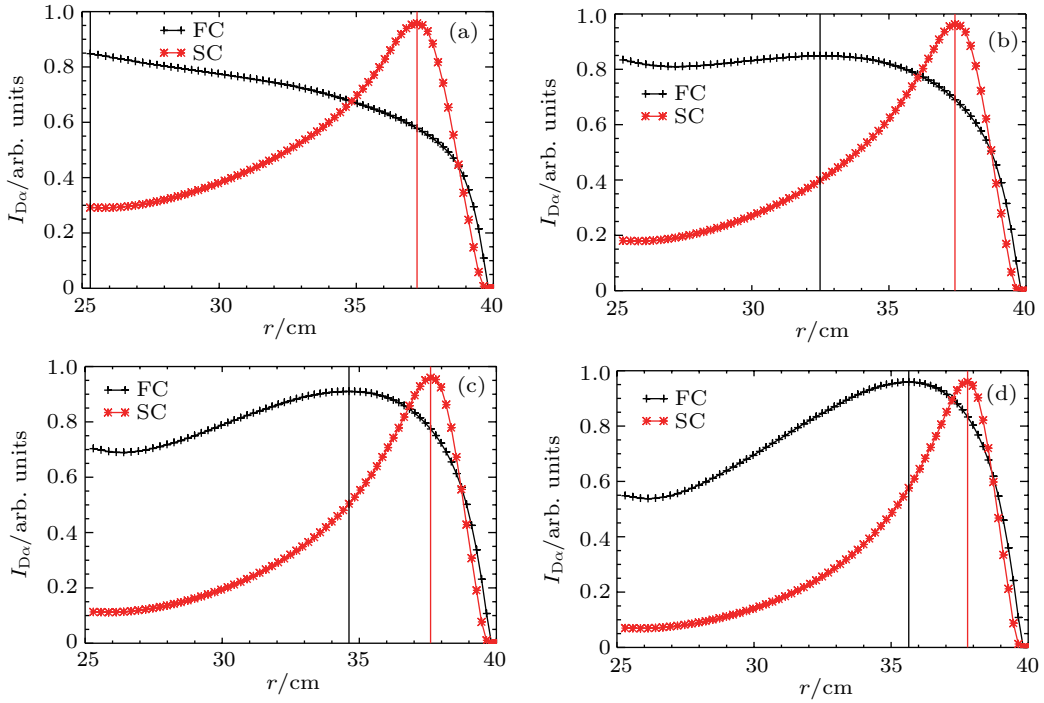


Fig. 6. (color online) Radial profiles of D_α intensity for FC and SC under different initial plasma densities. At the inner boundary of the simulation domain $r = 25$ cm, the plasma density (a) $N_i = 0.6N_0$, (b) $N_i = 1.0N_0$, (c) $N_i = 1.5N_0$, (d) $N_i = 2.0N_0$.

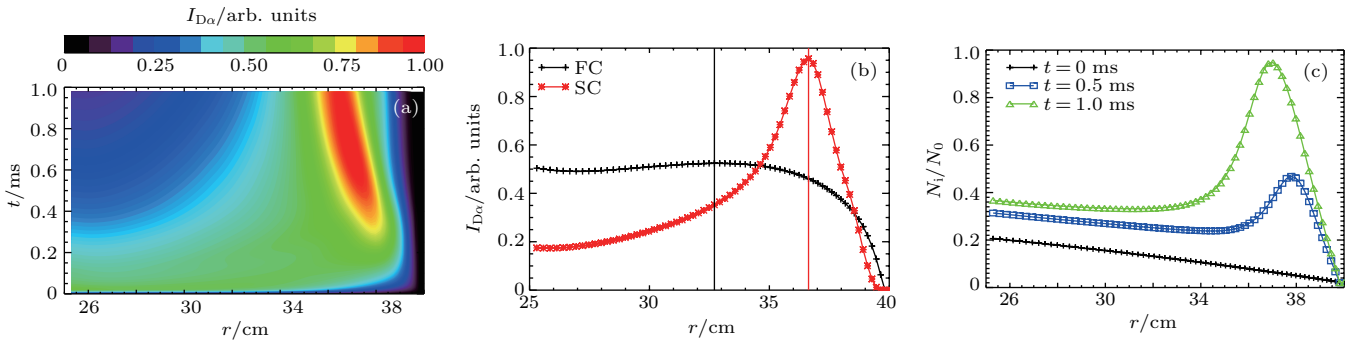


Fig. 7. (color online) Simulation verification of the influence of the self-blocking effect on the penetration depth of SMBI. (a) The spatio–temporal evolution of D_α intensity during SMBI. (b) Radial profiles of D_α intensity for the FC and SC, respectively. (c) Evolution of the radial profile of plasma density at the injection path.

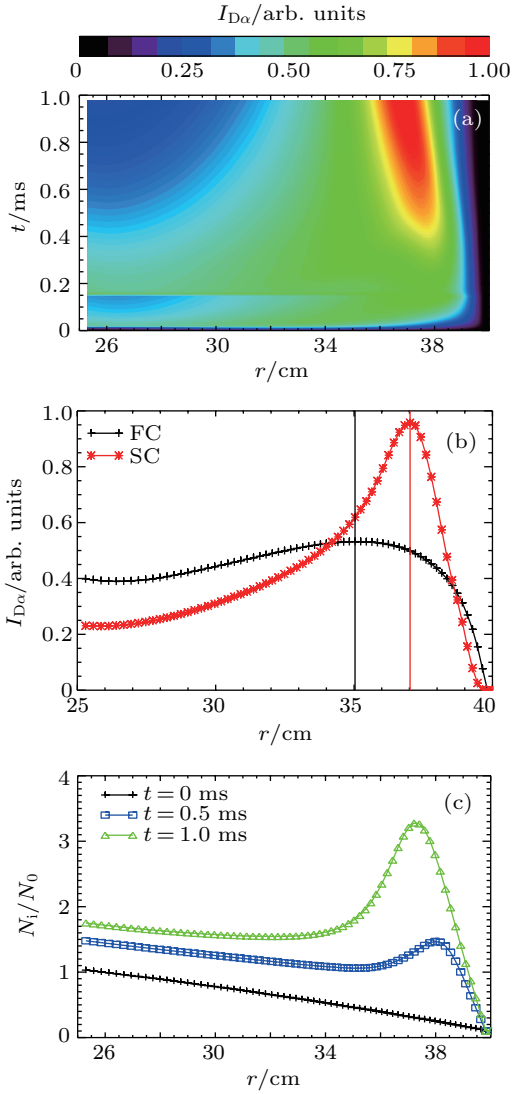


Fig. 8. (color online) Further verification of the influence of the self-blocking effect on the penetration depth of SMBI. (a) The spatio–temporal evolution of D_α intensity during SMBI. (b) Radial profiles of D_α intensity for the FC and SC, respectively. (c) Evolution of the radial profile of plasma density at the injection path.

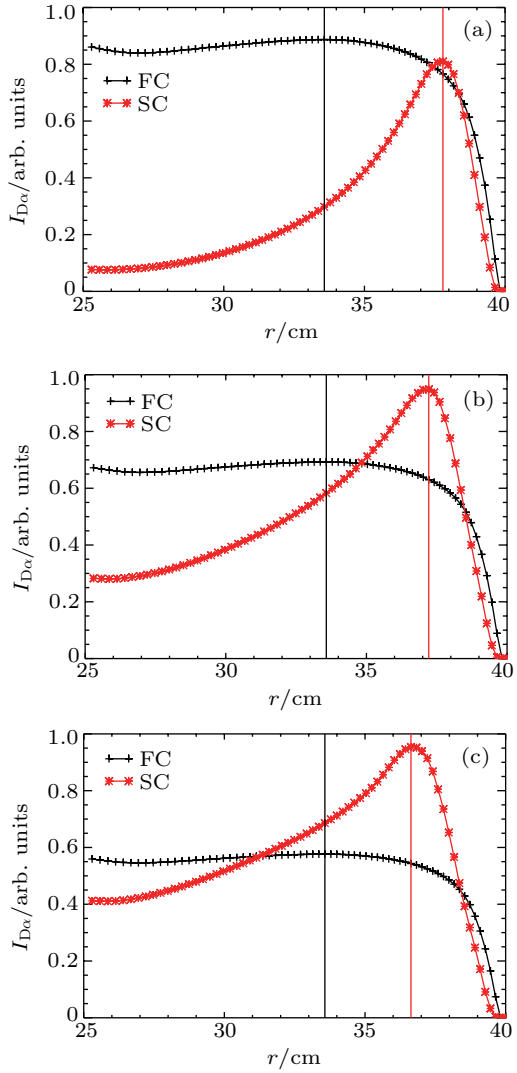


Fig. 9. (color online) The penetration depth of SC improved with the increases of the injection velocity. Radial profiles of D_α intensity for the FC and SC with injection velocities of (a) 500 m/s, (b) 1200 m/s, (c) 1800 m/s.

4.5. Effect of the injection velocity on SC

Since the proportion of the FC is small and its advantage in the penetration depth diminishes gradually with the increase of the plasma density, the penetration depth of SMBI is mainly determined by the SC. Therefore, in order to promote the penetration effect of SMBI, the penetration depth of the SC needs to be improved first. Because the penetration depth of the SC remains almost invariant with different plasma densities, we try to simulate the influence of the injection velocity on the SC penetration depth. The simulation results are shown in Fig. 9. Figures 9(a)–9(c) show the D_α intensity induced by the FC and SC with velocities of 500 m/s, 1200 m/s and 1800 m/s, respectively. We can see from Fig. 9 that the penetration depth of the SC is gradually improved with the increase of the injection velocity, but it is still much shallower than the FC.

5. Summary

It is very important to improve the penetration depth and the fueling efficiency of supersonic molecular beam injection (SMBI) especially for the next generation fusion devices such as ITER. Two components, a fast component and a slow component, are observed in the HL-2A SMBI experiments, and the FC can penetrate much deeper than the common SMBI does. It is the observation of the FC that greatly draws our attention to develop a new method of SMBI with deeper penetration and higher efficiency. In this paper, we have first studied and interpreted the FC and SC of SMBI on the HL-2A tokamak with the trans-neut module of the BOUT++ code. The FC and SC are observed and realized in the simulation, which are qualitatively consistent with the experimental results. The principal simulation results are summarized as follows. (i) The penetration depth difference between the FC and SC is mainly caused by the self-blocking effect of the first ionized atoms on the following ones due to the highly increased plasma den-

sity, though the injection speed may also influence the injection depths of the FC and SC. (ii) The influence of the initial plasma density on the FC and SC has been discussed. The penetration depth of the FC becomes shallower with the increase of the plasma density due to the larger ionization rate, but the penetration depth of the SC keeps almost invariant. (iii) The penetration depth of the SC is gradually improved with the increase of the injection velocity, but it is still much shallower than the FC. We should find a way to reduce the self-blocking effect by developing a new technology to make a little-transient-dense SMBI pulse (like a pellet) on tens of microseconds before the blocking effect turns on.

Acknowledgments

The authors wish to thank X Q Xu, B D Dudson, and M V Umansky for their contributions to the BOUT++ framework. The authors would also like to thank Zengchen Yang, Chengyuan Chen, Ting Long, Yulin Zhou, and Lin Nie for their valuable discussions and suggestions.

References

[1] Baylor L R, Jernigan T C, Combs S K, Houlberg W A, Murakami M, Gohil P, Burrell K H, Greenfield C M, Groebner R J, Hsieh C L, La Haye R J, Parks P B, Staebler G M, Staebler G M, DIII-D term, Schmidt G L, Ernst D R, Synakowski E J and Porkolab M 2000 *Phys.Plasmas* **7** 1878

[2] Sajjad S, Gao X, Ling B, Bhatti S H and Ang T 2009 *Phys. Lett. A* **373** 1133

[3] YAO L H, Zhao D W, Feng B B, Chen C Y, Zhou Y, Han X Y, Li Y G, Jerome B and Duan X R 2010 *Plasma Sci. Technol.* **12** 529

[4] Yu D L, Chen C Y, Yao L H, Dong J Q, Feng B B, Zhou Y, Shi Z B, Zhou J, Han X Y, Zhong W L, Cui C H, Huang Y, Cao Z, Liu Yi, Yan L W, Yang Q W, Duan X R and Liu Yong 2012 *Nucl. Fusion* **52** 082001

[5] Yao L H, Feng B B, Chen C Y, Shi Z B, Yuan B S, Zhou Y, Duan X R, Sun H J, Lu J, Jiao Y M, Ni G Q, Lu H Y, Xiao W W, Li W, Pan Y D, Hong W Y, Ran H, Ding X T and Liu Y 2007 *Nucl. Fusion* **47** 1399

[6] Guirlet R, Villegas D, Parisot T, Bourdelle C, Garbet X, Imbeaux F, Mazon D and Pacella D 2009 *Nucl. Fusion* **49** 055007

[7] Cui X W, Cui Z Y, Feng B B, Pan Y D, Zhou H Y, Sun P, Fu B Z, Lu P, Dong Y B, Gao J M, Song S D and Yang Q W 2013 *Chin. Phys. B* **22** 125201

[8] Zhou H Y, Cui Z Y, Morita S, Fu B Z, Goto M, Sun P, Feng B B, Cui X W, Lu P and Yang Q W 2014 *Plasma Sci. Technol.* **16** 89

[9] Xiao W W, Zou X L, Ding X T, Yao L H, Feng B B, Song X M, Song S D, Zhou Y, Liu Z T, Yuan B S, Sun H J, Ji X Q, Gao Y D, Li Y G, Yan L W, Yang Q W, Liu Yi, Dong J Q, Duan X R, Liu Y and Pan C H 2010 *Phys. Rev. Lett.* **104** 215001

[10] Duan X R, Dong J Q, Yan L W, *et al*. 2010 *Nucl. Fusion* **50** 095011

[11] Miki K, Diamond P H, Hahn S H, Xiao W W, Gürcan Ö D and Tynan G R 2013 *Phys. Rev. Lett.* **110** 195002

[12] Xiao W W, Diamond P H, Zou X L, *et al*. 2012 *Nucl. Fusion* **52** 114027

[13] Xiao W W, Diamond P H, Kim W C, *et al*. 2014 *Nucl. Fusion* **54** 023003

[14] Rhee T, Kwon J M, Diamond P H and Xiao W W 2012 *Phys. Plasmas* **19** 022505

[15] Kim J, Jeon Y M, Xiao W W, Yoon S W, Park J K, Yun G S, Ahn J W, Kim H S, Yang H L and Kim H K 2012 *Nucl. Fusion* **52** 114011

[16] Kwak J G, Oh Y K, Yang H L, *et al*. 2013 *Nucl. Fusion* **53** 104005

[17] Lee H Y, Hahn S H, Ghim Y C, Bak J G, Lee J H, Ko W H, Lee K D, Lee S H, Lee H H, Juhn J W, Kim H S, Yoon S W, Han H, Hong J H, Jang J H, Park J S and Choe W 2015 *Phys. Plasmas* **22** 122512

[18] Yang Z C, Shi Z B, Zhong W L, Zhang B Y, Fan Q C, Li H D, Jiang M, Shi P W, Chen C Y, Chen W, Liu Z T, Yu D L, Zhou Y, Feng B B, Song X M, Ding X T, Yang Q W, Duan X R and HL-2A Team 2016 *Phys. Plasmas* **23** 012515

[19] Sun H J, Ding X T, Yao L H, Feng B B, Liu Z T, Duan X R and Yang Q W 2010 *Plasma Phys. Control. Fusion* **52** 045003

[20] Sun H J, Diamond P H, Shi Z B, Chen C Y, Yao L H, Ding X T, Feng B B, Huang X L, Zhou Y, Zhou J, Song X M and the HL-2A team 2011 *Nucl. Fusion* **51** 113010

[21] Pan O, Xu Y, Hidalgo C, Zhong W L, Shi Z B, Ji X Q, Jiang M, Feng B B, Zhou Y, Cheng J, Liu Y, Xu M, Chen W, Ding X T, Yan L W, Yang Q W, Duan X R, Liu Y and the HL-2A team 2015 *Nucl. Fusion* **55** 113010

[22] Ida K, Shi Z, Sun H J, *et al*. 2015 *Nucl. Fusion* **55** 013022

[23] Yu D L, Chen C Y, Yao L H, Feng B B, Han X Y, Yang L M, Zhong W L, Zhou Y, Zhao K J, Huang Y, Liu Y, Yan L W, Yang Q W, Dong J Q and Duan X R 2010 *Nucl. Fusion* **50** 035009

[24] Yao L H, Zhao D W, Feng B B, Chen C Y, Zhou Y, Han X Y, Li Y G, Jerome B and Duan X R 2010 *Plasma Sci. Technol.* **12** 529

[25] Shi Z B, Ding X T, Yao L H, Liu Z T, Chen Ch Y, Yang Q W, Feng B B, Zhou Y, Yan L W, Liu Y and Liu Y 2005 *Plasma Phys. Control. Fusion* **47** 2019

[26] Dong J F, Tang N Y, Li W, Luo J L, Liu Y, Xiao Z G, Yao L H, Feng B B, Li B and Qin Y W 2002 *Plasma Phys. Control. Fusion* **44** 371

[27] Yao L H, Dong J F, Zhou Y, Feng B B, Cao J Y, Li W, Feng Z, Zhang J Q, Hong W Y, Cui Z Y, Wang E Y and Liu Y 2004 *Nucl. Fusion* **44** 420

[28] Takenaga H and the JT-60 Team 2009 *J. Nucl. Mater.* **390–391** 869

[29] Takenaga H, Miyo Y, Bucalossi J, Marty V, Urano H, Asakura N, Nishiyama T, Sasajima T, Masaki K and Kaminaga A 2010 *Nucl. Fusion* **50** 115003

[30] Dudson B D, Umansky M V, Xu X Q, Snyder P B and Wilson H R 2010 *Comput. Phys. Commun.* **180** 1467

[31] Wang Z H, Xu X Q, Xia T Y and Rognlien T D 2014 *Nucl. Fusion* **54** 043019

[32] Wang Z H, Xu X Q, Xia T Y, Yu D L, Zheng G Y, Huang J, Chen S Y, Zhong W L, Shi Z B, Sun A P, Dong J Q, Xu M , Sun T T and Yao L H 2014 *25th IAEA Fusion Energy Conference* TH/P7-30

[33] Zhou Y L, Wang Z H, Xu X Q, Li H D, Feng H and Sun W G 2015 *Phys. Plasmas* **22** 012503

[34] Zhou Y L, Wang Z H, Xu X Y, Li H, Feng H H and Sun W G 2016 *Chin. Phys. B* **25** 095201

[35] Wang Y H, Guo W F, Wang Z H, Ren Q L, Sun A P, Xu M, Wang A K and Xiang N 2016 *Chin. Phys. B* **25** 106601

[36] Summers H P 2000 *The ADAS User Manual* (version 2.2) http://adas.phys.strath.ac.uk

[37] Braginskii S.I. 1965 *Reviews of Plasma Physics* Vol. 1 (Leontovich M A, Ed.) (New York: Consultants Bureau) p. 205